Nitrogen-Doped Porous Co$_3$O$_4$/Graphene Nanocomposite for Advanced Lithium-Ion Batteries

Huihui Zeng [1], **Baolin Xing [1,2,]***, **Lunjian Chen [1]**, **Guiyun Yi [1]**, **Guangxu Huang [1]**, **Ruifu Yuan [1]**, **Chuanxiang Zhang [1,]***, **Yijun Cao [2]** and **Zhengfei Chen [3]**

[1] Henan Key Laboratory of Coal Green Conversion, College of Chemistry and Chemical Engineering, Henan Polytechnic University, Jiaozuo 454003, China
[2] Henan Province Industrial Technology Research Institute of Resources and Materials, Zhengzhou University, Zhengzhou 450001, China
[3] Laboratory of Polymer Materials and Engineering, Ningbo Institute of Technology, Zhejiang University, Ningbo 315100, China
* Correspondence: baolinxing@hpu.edu.cn (B.X.); zcx223@hpu.edu.cn (C.Z.);
  Tel.: +86-0391-3986922 (B.X.); +86-0391-3986816 (C.Z.)

check for updates

Abstract: A novel approach is developed to synthesize a nitrogen-doped porous Co$_3$O$_4$/anthracite-derived graphene (Co$_3$O$_4$/AG) nanocomposite through a combined self-assembly and heat treatment process using resource-rich anthracite as a carbonaceous precursor. The nanocomposite contains uniformly distributed Co$_3$O$_4$ nanoparticles with a size smaller than 8 nm on the surface of porous graphene, and exhibits a specific surface area (120 m^2·g^{-1}), well-developed mesopores distributed at 3~10 nm, and a high level of nitrogen doping (5.4 at. %). These unique microstructure features of the nanocomposite can offer extra active sites and efficient pathways during the electrochemical reaction, which are conducive to improvement of the electrochemical performance for the anode material. The Co$_3$O$_4$/AG electrode possesses a high reversible capacity of 845 mAh·g^{-1} and an excellent rate capacity of 587 mAh·g^{-1}. Furthermore, a good cyclic stability of 510 mAh·g^{-1} after 100 cycles at 500 mA·g^{-1} is maintained. Therefore, this work could provide an economical and effective route for the large-scale application of a Co$_3$O$_4$/AG nanocomposite as an excellent anode material in lithium-ion batteries.

Keywords: Co$_3$O$_4$ nanoparticles; anthracite-derived graphene; nanocomposite; lithium-ion batteries

1. Introduction

Rechargeable batteries play a crucial part in portable electronic devices and electromobiles as energy storage and conversion devices [1]. Lithium-ion batteries (LIBs) have drawn extensive concern owing to their high energy density, long cycling life, high power, and safety [2,3]. In LIBs, the anode material is one of many factors that can affect their ultimate performance [4,5]. However, the current graphite anode with a low theoretical capacity (372 mAh·g^{-1}) limits the performance improvement of LIBs [6]. Therefore, it is highly necessary to explore new advanced anode material for a new generation of LIBs.

Many transition metal oxides [7–10] show potential as promising anode candidates for LIBs by reason of their better theoretical capacity, high power density, and easy accessibility [11,12]. Among these materials, Co$_3$O$_4$ is a potential anti-ferromagnetic p-type semiconductor with a spinel crystal structure, which can coordinate with eight lithium ions per single lattice and deliver a higher theoretical capacity of 890 mAh·g^{-1} [13,14]. Unfortunately, pure Co$_3$O$_4$ as an anode is subjected to a poor cycling stability and rate capability because of its poor electronic conductivity, and the

pulverization or agglomeration of primitive particles during charging/discharging processes [15]. Generally, engineering nanostructured Co_3O_4 and preparing Co_3O_4 composites are considered to heighten the structural stability and enhance the properties of the Co_3O_4 anode. It is universally accepted that the nanostructure and morphology of the Co_3O_4 are significant to avoid electrical isolation of the electrode due to the Li_2O produced during the conversion process [16,17]. In line with this hypothesis, a series of studies on engineering various nanostructured Co_3O_4, such as nanoparticles [18], nanosheets [19], and microfibers [20], have been subsequently carried out. Although the property of these nanostructured Co_3O_4 as an anode in LIBs has been improved, the complex process and high cost for preparing these Co_3O_4 are hurdles for practical applications.

Co$_3$O$_4$/carbon composites, such as Co_3O_4/carbon nano-onions [21], Co_3O_4/carbon nanotube [22], Co_3O_4/porous carbon [23], and Co_3O_4/graphene hybrid [4], are potentially anode materials for LIBs. Among numerous materials, Co_3O_4/graphene composites have attracted extensive research due to their unique structural advantages [15]: firstly, the superior electronic conductivity of graphene can shorten the path length to facilitate faster lithium ion and electron diffusion; secondly, graphene has a large theoretical capacity (744 mAh·g^{-1}) as it can provide additional reactive sites for lithium ion storage [24]; thirdly, the structural flexibility and large specific surface area of graphene can offer adequate void spaces to relieve the large volume expansion of Co_3O_4 nanoparticles during charging/discharging processes; and lastly, the agglomeration of Co_3O_4 nanoparticles may be prevented when they are evenly dispersed on the surface of graphene. However, employing 2D structural graphene as a substrate does not significantly improve the electrochemical property of Co_3O_4 because of the easy aggregation of the graphene nanosheets on account of the van der Waals interactions among these nanosheets [25]. As a result, some research effort has been made to construct 3D Co_3O_4/graphene using copper foam as a template in order to overcome this shortcoming [26]. However, this process is very complicated, limiting its use in commercial applications.

In line with this, coal may be a desirable material to prepare porous graphene, because it contains abundant polyaromatic structures like sp^2 bonding structures, which are cross-linked via some oxygen-containing functional groups [27]. There are some literature reports on the preparation of graphene electrodes with a high performance from various coals, such as 3D graphene from coal tar pitch [28] and graphene/Mn$_3$O$_4$ composites from coal-derived graphite [29]. Recently, our group investigated the preparation of porous graphene by a graphitization process, followed by an oxidation-thermal treatment approach [30]. These works have demonstrated that using coal as a raw material to prepare porous graphene is feasible, but the practical application of graphene is still limited due to its high irreversible capacity [2].

In this work, we report an economical and effective approach to fabricate a nitrogen-doped porous Co_3O_4/anthracite-derived graphene (Co_3O_4/AG) nanocomposite using the earth-abundant and low-cost anthracite as a carbonaceous precursor. The anthracite was firstly graphitized to obtain a highly lamellar structure and was then converted into anthracite-derived graphene oxide (AGO) by a modified Hummers method. Next, the AGO was used as a carbon source to synthesize the nitrogen-doped porous Co_3O_4/AG nanocomposites by self-assembly, followed by a heat treatment method. The crystal structure and composition, porous morphology structure, surface chemical property, and electrochemical performances of these samples were systematically investigated. This nanocomposite contained crystalline Co_3O_4 nanoparticles, which were evenly dispersed on the surface of porous graphene and had a large surface area, displaying a much better electrochemical performance as an anode in LIBs.

2. Materials and Methods

2.1. Preparation of AGO

The powdered anthracite sample from the Ningxia region in China was firstly carbonized at 1000 °C under argon atmosphere, followed by further graphitization at 2800 °C, to obtain synthetic

graphite. Then, the flocculent AGO was prepared via a modified Hummers method following our previous work [30].

2.2. Synthesis of Co₃O₄/AG Nanocomposite

The Co_3O_4/AG nanocomposite was synthesized via self-assembly, followed by a heat treatment method. In detail, 1 g of AGO was completely dispersed in 150 mL aqueous solution by ultrasound treatment for 1 h. After that, 50 mL of 10 mg/mL $Co(NO_3)_2 \cdot 6H_2O$ was slowly dropped into the AGO suspension drop-wise under continuous stirring, followed by the addition of 10 mL 28 wt. % ammonium hydroxide ($NH_3 \cdot H_2O$). This mixture was continuously stirred for 2 h to produce cobalt hydroxide and to allow the self-assembly Co_3O_4 nanoparticles on AGO. After the reaction, the Co_3O_4/AG nanocomposite precursor was dried through freeze-drying and then further calcined at 500 °C for 2 h under N_2 atmosphere, and the final Co_3O_4/AG nanocomposite was obtained after grinding. The synthetic process of the Co_3O_4/AG nanocomposite is illustrated in Figure 1. For comparison purposes, Co_3O_4 nanoparticles were prepared via the same process, without the addition of AGO, and anthracite-derived graphene (AG) was obtained using AGO as a raw material by the same calcination method.
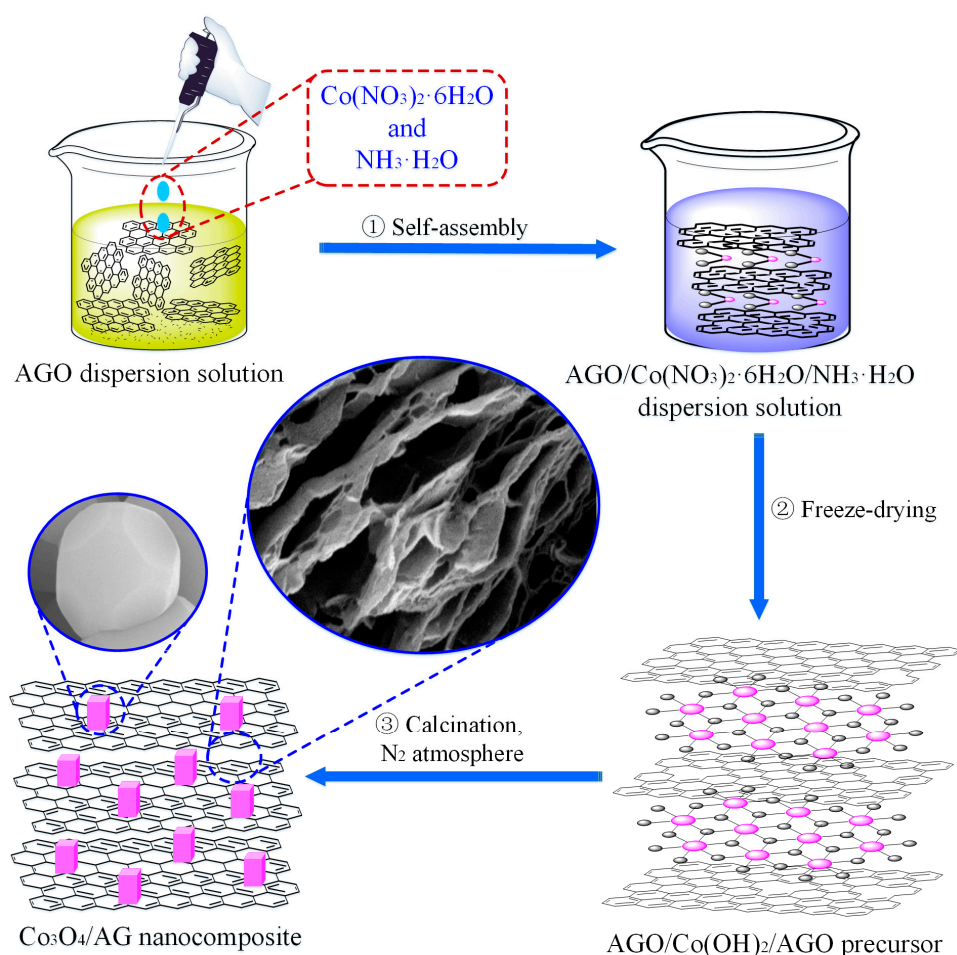

Figure 1. Schematic illustration of the synthetic process of the Co_3O_4/AG nanocomposite.

2.3. Material Characterization

The X-ray diffraction (XRD, Bruker, Karlsruhe, Germany) patterns of Co_3O_4, AG, and the Co_3O_4/AG nanocomposite were recorded by a D8 Advance instrument (Cu Kα radiation, λ = 0.15418 nm) at the range of 10–80°, and the Raman spectra were acquired on an inVia Raman spectroscope (Renishaw, London, UK, Ar ion laser, λ = 514 nm) from 2400 to 200 cm^{-1}. A Quanta FEG 250 scanning electron microscopy (SEM, FEI, Hillsboro, Oregon, USA) and one JEM-2100 transmission electron microscope

(TEM, JEOL, Tokyo, Japan) were employed to observe the morphological structure. The N_2 adsorption measurement was conducted on an Autosorb-iQ-MP instrument (Quantachrome, Norcross, GA, USA) at $-196\,°C$. Meanwhile, the Brunauer–Emmett–Teller (BET) model was applied to evaluate the specific surface area of AG and the Co_3O_4/AG nanocomposite. The X-ray photoelectron spectroscopy (XPS, Thermo Fisher Scientific, Waltham, MA, USA) analyses were measured by an Escalab 250Xi instrument (Al Kα radiation, 1486.6 eV) to confirm the chemical composition of samples. Lastly, the thermogravimetric (TG, Netzsch, Bavaria, Germany) analysis of the nanocomposite was studied on a STA409 PC thermogravimetric analyzer under air flow (30–$700\,°C$, $10\,°C\,min^{-1}$).

2.4. Electrochemical Measurements

Electrochemical measurements were evaluated by a coin-type cell (CR2016, Jinghong, Zhengzhou, China). The working electrodes were constructed by mixing 80 wt. % as-prepared samples, 10 wt. % acetylene black, and 10 wt. % polyvinyldene fluoride (PVDF, Aladdin, Shanghai, China) in N-methylpyrrolidone (NMP, Aladdin, Shanghai, China) to form slurry and the mixed slurry was then uniformly painted onto copper foil. After drying at $105\,°C$ under vacuum, some disks with a diameter of 14 mm were obtained from the painted copper foil. Besides, pure lithium foil and a polypropylene microporous film (Celgard 2400) were employed as a separator and counter electrode, and 1M $LiPF_6$ in ethylene carbonate/dimethyl carbonate (1:1 vol. ratio) was applied as the electrolyte. A BTS-3000n test instrument (Neware, Shenzhen, China) was employed for galvanostatic charge/discharge measurements, with a voltage window from 0.01 to 3.0 V (vs. Li/Li$^+$). Cyclic voltammetry (CV) was carried out on a CHI660D workstation (Chenhua, Shanghai, China). Electrochemical impedance spectroscopy (EIS) was conducted on a Parstat 2273 workstation (Princeton applied research, Oak ridge, TN, USA) in a frequency range of 100 to 0.01 Hz.

3. Results and Discussion

3.1. Material Characterization

The phase compositions of Co_3O_4, AG, and the Co_3O_4/AG nanocomposite were analyzed by XRD patterns, as shown in Figure 2a. For Co_3O_4, the main diffraction peaks at 19.0°, 31.3°, 36.7°, 44.7°, 59.4°, and 65.4° can be respectively assigned to (111), (220), (311), (400), (511), and (440) crystal planes (JCPDS 42-1467) [18]. The Co_3O_4/AG nanocomposite contains only the diffraction peaks of Co_3O_4 and AG (the (002) peak at around 26°), confirming that the Co_3O_4 nanoparticles in the sample have excellent crystallinity and AGO was reduced to AG during the synthetic process of the nanocomposite. Furthermore, the structures of these samples were evaluated by Raman spectra, as demonstrated in Figure 2b. For Co_3O_4, the four peaks at 470, 513, 608, and 676 cm^{-1} correspond to the E$_g$, F$_{2g}$, F$_{2g}$, and A$_{1g}$ modes of spinel Co_3O_4, separately [31]. The AG sample shows a D and G band at around 1343 and 1589 cm^{-1}, which correspond to the characteristics of defect sites and a disordered structure, and the features of ordered few-layer graphene, respectively [32]. As expected, the Co_3O_4/AG nanocomposite has a combination of peaks from Co_3O_4 and AG. Meanwhile, it can be found that the Co_3O_4/AG nanocomposite shows a relatively larger intensity ratio of the D band to the G band (I$_D$/I$_G$ = 1.02) than that of AGO (I$_D$/I$_G$ = 0.96), indicating that more structural defects exist in the nanocomposite after calcination. However, the I$_D$/I$_G$ value of the nanocomposite is lower than that of AG (I$_D$/I$_G$ = 1.18), suggesting that Co_3O_4 has impacted the formation of structural defects in AG during the synthetic process of the nanocomposite. It is commonly accepted that some defects in a nanocomposite can provide more active sites, which are conductive to storing more lithium ions for a high capacity [33]. Therefore, the Co_3O_4/AG nanocomposite may act as a potential candidate for a high-performance anode in LIBs.
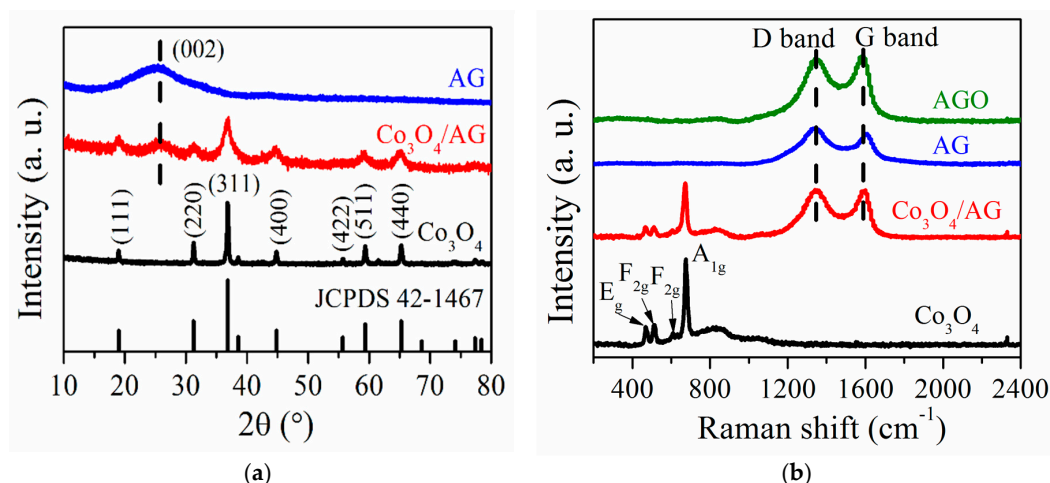
Figure 2. XRD patterns (**a**) and Raman spectra (**b**) of Co_3O_4, AG, and the Co_3O_4/AG nanocomposite.

The microstructure characteristics of AG and the Co_3O_4/AG nanocomposite are exhibited in Figure 3. The AG sample (Figure 3a) shows a continuous wrinkled sheet-like structure, and these nanosheets are interconnected to construct a 3D porous structure with abundant nanoscale pores. After the Co_3O_4 nanoparticles were dispersed onto these nanosheets, the morphologies and structure of the nanocomposite could be seen, as shown in Figure 3b–d. The SEM images (Figure 3b,c) at a lower magnification exhibit a lot of wrinkled AG nanosheets with a porous structure and the three-dimensional porous structure in the nanocomposite can be clearly observed at a higher magnification (Figure 3d). The element mapping of the sample (Figure 3e) suggests that the C, O, Co, and N elements are evenly existent in the nanocomposite, suggesting that the finer-grained Co_3O_4 are well-dispersed on the surface of AG. The energy dispersive spectrometer (EDS) profile (Figure 3f) confirms that the nanocomposite is only comprised of C, O, Co, and N elements. Besides, the TEM micrograph (Figure 3g) also demonstrates that the AG sample has a wrinkled sheet-like structure composed of several layers. For the TEM image of the nanocomposite in Figure 3h, it can be observed that the Co_3O_4 nanoparticles are homogeneously dispersed onto the wrinkled AG nanosheets. The high resolution transmission electron microscope (HRTEM) image (Figure 3i) reveals that the Co_3O_4 nanoparticles with a size smaller than 8 nm are distributed on the surface of AG, and the interplanar distance is 0.286 nm, corresponding to the (220) plane of Co_3O_4 nanoparticles [34].

The nitrogen adsorption and desorption isotherms of AG and the Co_3O_4/AG nanocomposite reveal their detailed porous structures, which are shown in Figure 4. These isotherms belong to a typical type IV structure with an obvious hysteresis loop, which indicates that the material contains a large amount of mesopore structures. For the AG sample (Figure 4a), it exhibits a wide mesopore size distribution from 3 to 25 nm and a small number of micropores at around 1.2 nm. After the addition of Co_3O_4 nanoparticles, the pore size distribution of the Co_3O_4/AG nanocomposite (Figure 4b) narrows down to the region of 3~10 nm, owing to the fact that some of the large pores are filled by Co_3O_4 nanoparticles. Accordingly, the specific surface area calculated by the BET model falls from 383 $m^2 \cdot g^{-1}$ for the AG to 120 $m^2 \cdot g^{-1}$ for the Co_3O_4/AG nanocomposite. Nevertheless, the specific surface area of this material is still better than that of the pure Co_3O_4 [35] and other Co_3O_4/graphene composites [36–38]. Such a porous structure and large surface of the product can not only protect the electrode from damage due to the volume change of Co_3O_4, but also effectively favor the rapid diffusion of lithium ions during the electrochemical reaction, which is conducive to improvement of the performance for the material as an anode in LIBs.
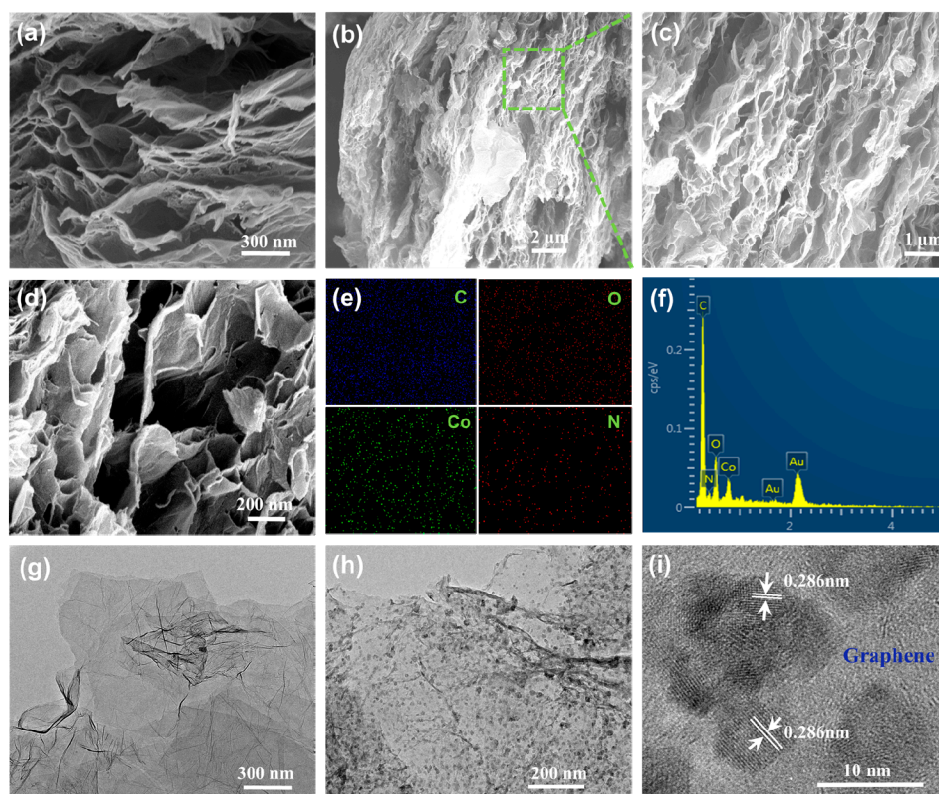
Figure 3. Microstructure characteristics of samples: (**a**) Scanning electron microscopy (SEM) images of AG, (**b–d**) SEM images of the Co_3O_4/AG nanocomposite, (**e**) and (**f**) elemental mapping and EDS of the Co_3O_4/AG nanocomposite, (**g**) and (**h**) transmission electron microscope (TEM) micrographs of AG and the Co_3O_4/AG nanocomposite, and (**i**) HRTEM micrograph of the Co_3O_4/AG nanocomposite.

(**a**)   (**b**)

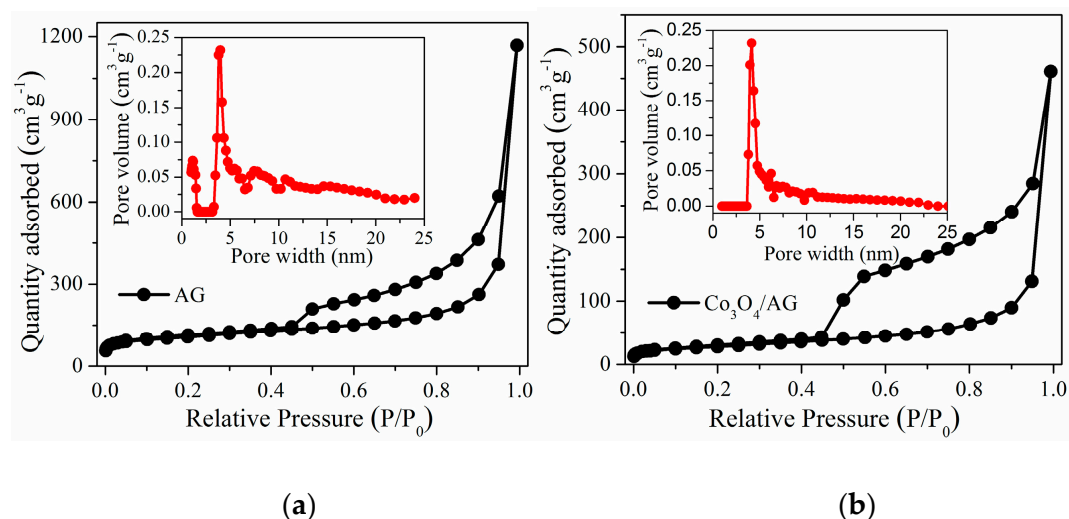**Figure 4.** Nitrogen adsorption and desorption isotherms (inset: pore size distribution) of samples: (**a**) AG and (**b**) the Co_3O_4/AG nanocomposite.

The surface chemistry of AG and the Co_3O_4/AG nanocomposite was investigated by XPS measurement, as shown in Figure 5a–e. The survey spectrum of AG (Figure 5a) demonstrates the existence of only C and O elements, whereas that of the nanocomposite contains Co, C, N, and O elements. This suggests that N atoms were introduced to the composite during the synthesis process, which resulted from the excess ammonium hydroxide which reacted with carbon atoms near defects and vacancies or oxygen functional groups in the AGO [39]. From Figure 5d, the N 1s spectrum could

be decomposed into three peaks (398.3, 399.6, and 401.2 eV), which could be ascribed to pyridinic (N1), pyrrolic (N2), and graphitic (N3) nitrogen atoms, separately. Meanwhile, XPS analysis shows that 5.4 at. % of nitrogen had been successfully doped into the Co_3O_4/AG nanocomposite. Because of its higher electronegativity of N (3.5) compared to C (3.0), the doped N could modify the graphene planar sheet and might play a crucial part in enhancing the electrochemical performance in LIBs [40]. In addition, the two binding energy peaks of Co2p at 796.3 and 780.9 eV shown in Figure 5b are respectively attributed to the spin effect of $Co2p_{1/2}$ and $Co2p_{3/2}$ electrons, which is in line with the reported Co_3O_4 [26]. From the high-resolution C1s spectrum (Figure 5c), the deconvoluted four peaks at 284.6, 285.1, 285.8, and 287.2 eV correspond to graphite-like sp^2 C, C-OH, N-sp^2 C, and sp^3 C [41], respectively. The O1s spectrum (Figure 5e) could be deconvoluted into three peaks, and the peaks at 530.4 and 531.9 eV were assigned to the lattice oxygen species in the Co_3O_4 and the oxygen in the OH– or C–O–C groups, separately [42]. Besides, the one at 533.4 eV belongs to the Co–O–C bond and C=O groups on the AG surface, indicating that the Co_3O_4 nanoparticles in the nanocomposite were anchored on the surface of AG sheets, which has been researched in detail in the literature [43]. Furthermore, the content of AG and Co_3O_4 in the Co_3O_4/AG nanocomposite was tested by TG measurement in Figure 5f. The weight loss (2.5%) below 150 °C is due to the loss of adsorbed water on the surface of the nanocomposite, and the weight loss at 150–450 °C is due to the decomposition and removal of oxygen functional groups. On the basis of the TG curve, it can be seen that the contents of AG and Co_3O_4 in the nanocomposite are about 62.4 wt. % and 35.1 wt. %, respectively [37].
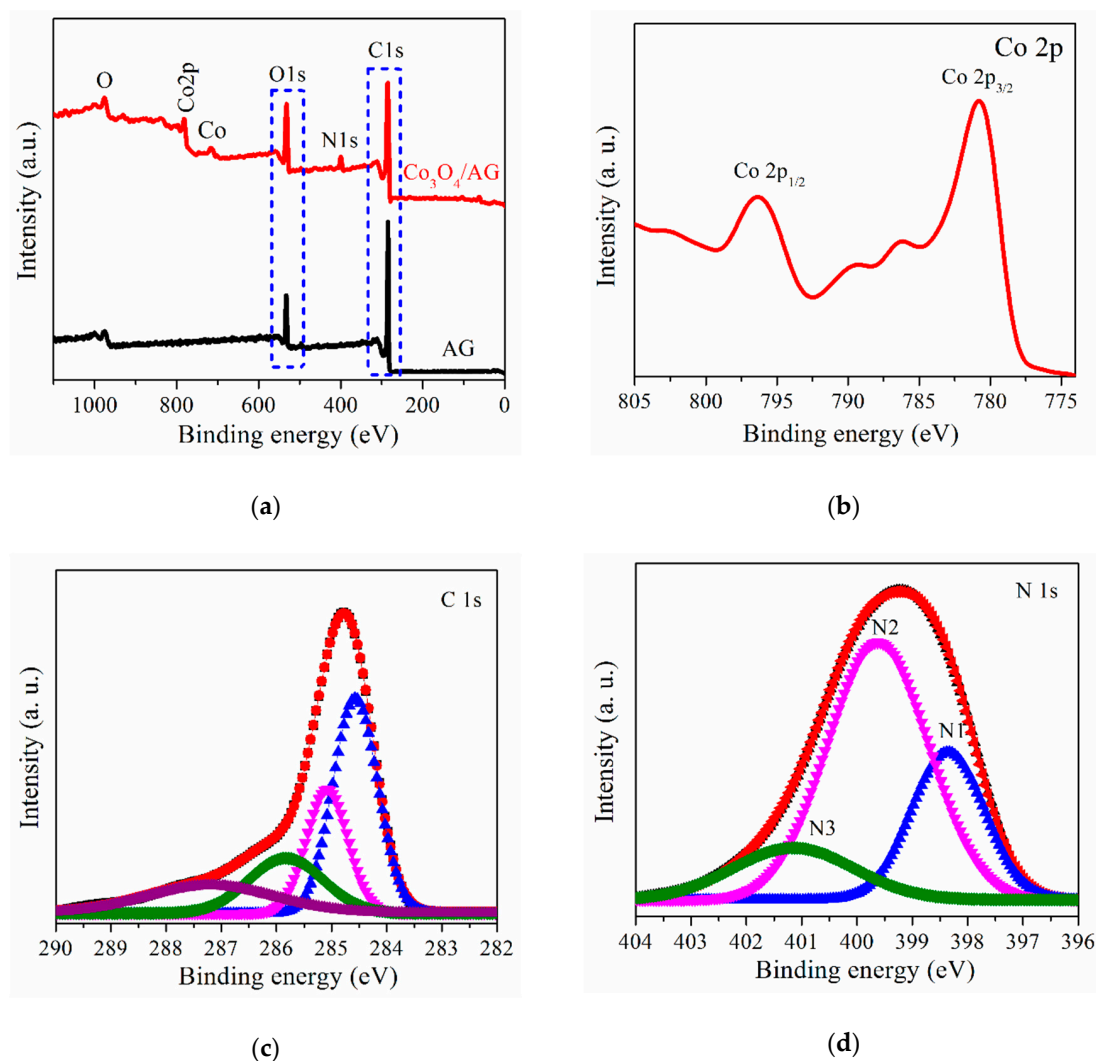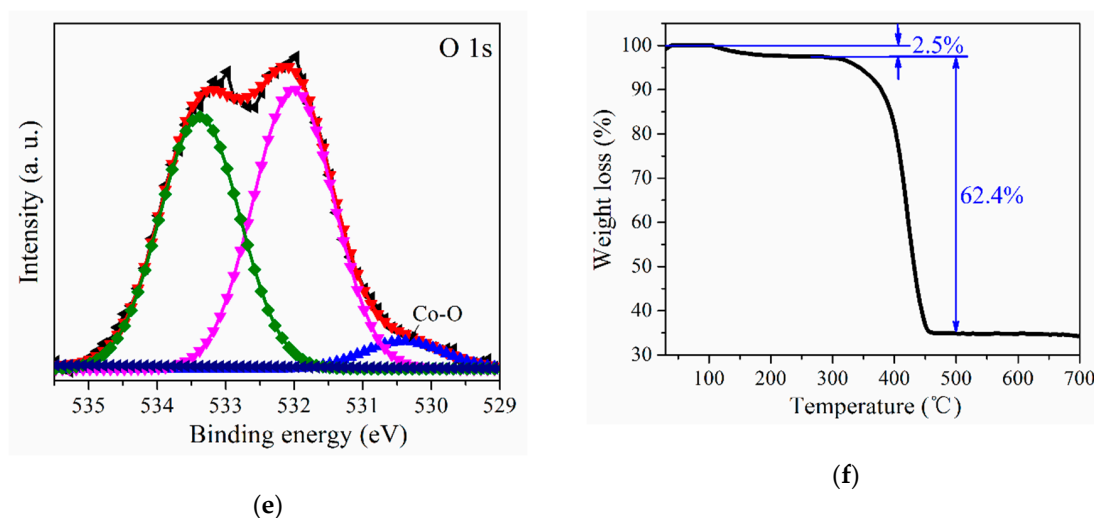

(a)

(b)

(c)

(d)

Figure 5. *Cont.*

(e)

(f)

Figure 5. XPS survey spectra and thermogravimetric (TG) curve of samples: (**a**) Wide scan spectra of AG and the Co_3O_4/AG nanocomposite; (**b**), (**c**), (**d**), and (**e**) high-resolution Co 2p, C 1s, N 1s, and O 1s spectra of the Co_3O_4/AG nanocomposite; (**f**) TG curve of the Co_3O_4/AG nanocomposite.

3.2. Electrochemical Performances

The CV scans of the Co_3O_4/AG nanocomposite at 0.1 mV·s^{-1} over the voltage range from 0.01 to 3.00 V were investigated, as shown in Figure 6a. During the first scan, one broad reduction peak can be found during 0.5–1.0 V, which is the initial reduction of Co_3O_4 along with the formation of amorphous Li_2O and solid electrolyte interphase (SEI) film [23]. The peak close to 0 V is deemed to arise from lithium ion intercalation into AG, indicating that AG in the material was also beneficial for lithium storage. The broad peaks at 1.30 and 2.20 V in the anodic scan were respectively attributed to the delithiation process of AG and the formation of CoO [44]. Electron energy loss spectroscopy (EELS) analysis showed that the white-line intensity ratio (L_3/L_2) after the first delithiation process corresponded to the valence state of 2+, which indicates that the oxidation product of metallic cobalt embedded in the Li_2O matrix is CoO rather than Co_3O_4. Meanwhile, such a CoO product was also confirmed by in situ TEM and the electron diffraction (ED) pattern [45]. Therefore, the electrochemical reaction of lithium-ions with Co_3O_4 is irreversible during the first cycle. During the second scan, two cathodic peaks at around 0.84 and 1.36 V can be observed, which corresponds to the decomposition process of SEI film and the reduction of CoO [46]. Compared to the peaks of the first scan, the anodic peaks at 1.30 and 2.20 V exhibit little change, suggesting a good reversibility during the charge/discharge reaction. Furthermore, the shape of the third scan is almost identical to that of the second one, which reveals that the cycling stability in the material is built after the first cycle.

To better understand the kinetic process, CV measurements at the scan rate of 0.2 to 2 mV·s^{-1} were carried out. The CV curves of the Co_3O_4/AG nanocomposite (Figure 6b) show obvious and well-defined redox peaks, which indicates that the conversion reactions of cobalt oxides with lithium have excellent kinetics [47]. If a redox reaction is controlled by semi-infinite diffusion, the relationship between the peak current (i) and the scan rate (v) is denoted as i = av^b, where the value of power coefficient b provides insight into the lithium-ion storage mechanism in the electrode [48]. Therefore, it could be obtained from Figure 6c that the logarithm of the current response (i) at 2.20 V for peak 1 exhibits a linear dependence with the logarithm of the sweep rate (v). The electrode kinetics that arose from surface-controlled behavior was confirmed by the value of power coefficient b (0.86), which is beneficial to and may facilitate the lithium-ion insertion/extraction processes [4].
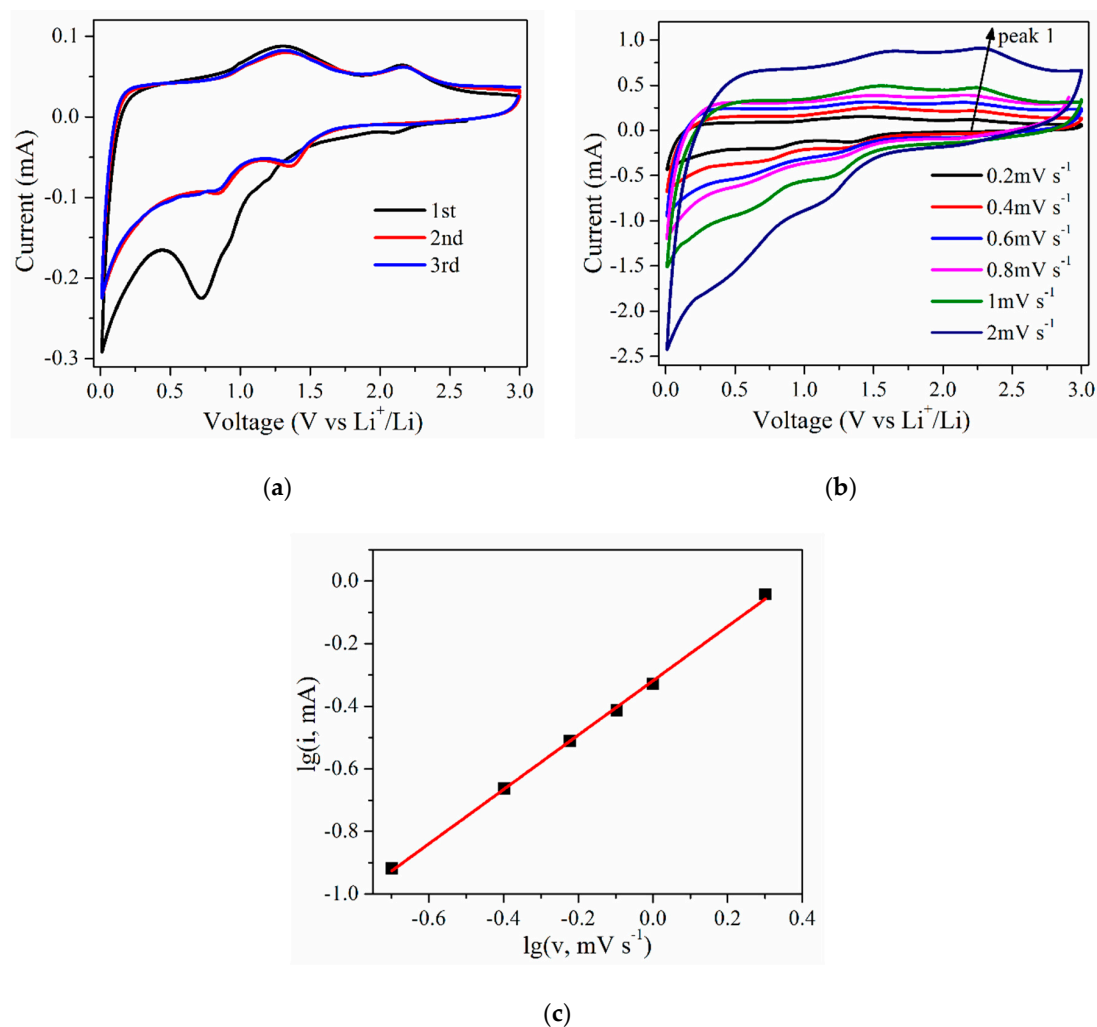
(a)

(b)

(c)

Figure 6. Cyclic voltammetry (CV) behavior of the Co_3O_4/AG nanocomposite: (**a**) CV curves at 0.1 mV·s^{-1}, (**b**) CV curves at various scan rates from 0.2 to 2 mV·s^{-1}, and (**c**) the relationship between the anodic peak current at around 2.20 V and the scan rate.

Figure 7a shows the galvanostatic charge/discharge behaviors of Co_3O_4, AG, and the Co_3O_4/AG nanocomposite at a current density of 100 mA·g^{-1} in a voltage range of 0.01 to 3.00 V (vs. Li/Li$^+$). The initial discharge and charge capacities of the nanocomposite electrode are 1388 and 845 mAh·g^{-1}, respectively, with the initial coulombic efficiency of 60.8%, which are superior to those of the Co_3O_4 electrode (463 and 444 mAh·g^{-1}, respectively) and importantly, the introduction of Co_3O_4 into the composite resulted in lower initial irreversible capacity loss compared to the AG electrode with the initial coulombic efficiency of 32.5%, corresponding to the initial discharge and charge capacities of 1467 and 478 mAh·g^{-1}, respectively. As for the Co_3O_4 electrode, the polarization (i.e., large voltage hysteresis) between the discharge and charge limited by lithium diffusion kinetics is the main factor of irreversible capacity loss [49]. Moreover, the reversible capacity of the nanocomposite is superior to the reported porous Co_3O_4/graphene [50], hollow Co_3O_4 nanoparticles [51], and Co_3O_4/graphene foams [52]. These suggest that AG with a porous structure can effectively improve the reversible capacity of pure Co_3O_4. In addition, the initial capacity loss for the nanocomposite is mainly due to the formative SEI film and the irreversible reaction between lithium-ions and the electrodes [53]. In the subsequent cycles, the Co_3O_4/AG nanocomposite likewise displays a much improved charge retention capacity compared to the Co_3O_4 and AG electrode.
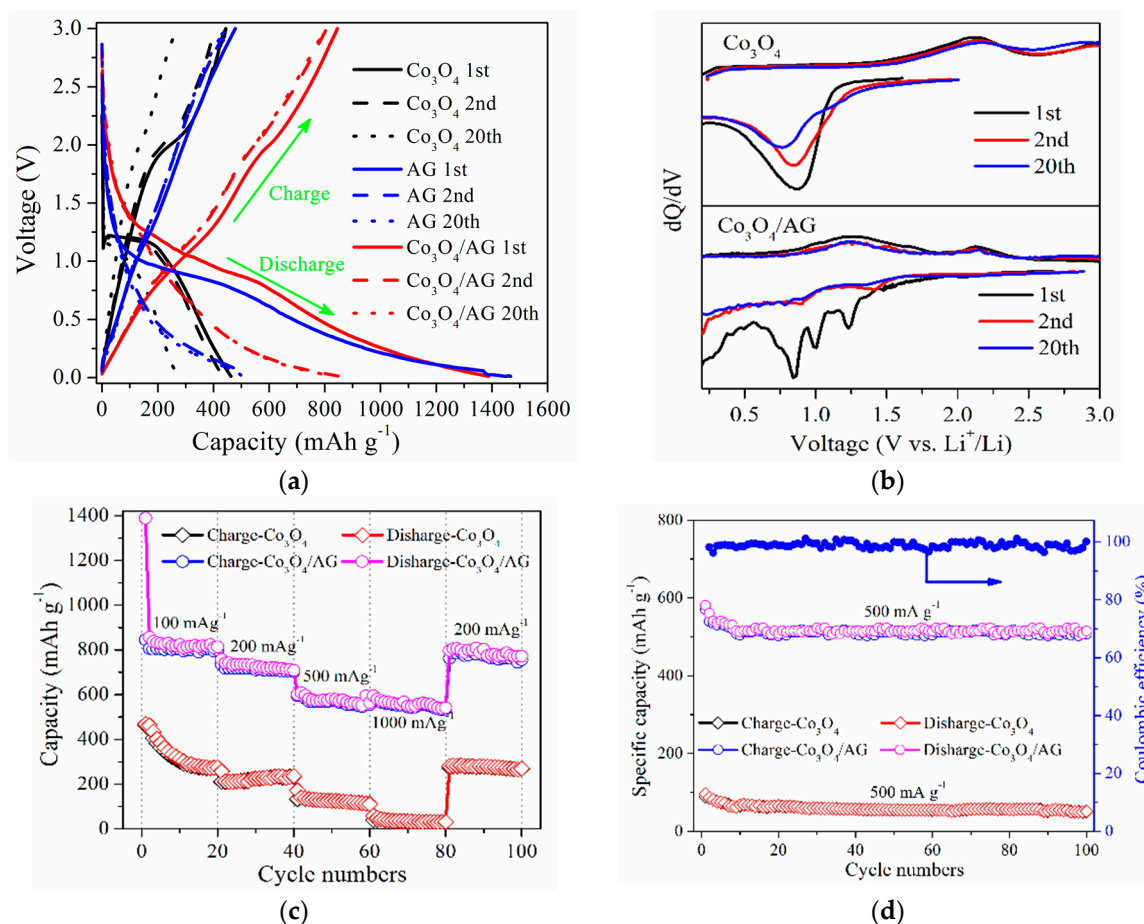
Figure 7. Electrochemical performances of Co_3O_4, AG, and the Co_3O_4/AG nanocomposite: (**a**) Galvanostatic charge/discharge curves, (**b**) differential capacity curves, (**c**) rate capability at various current densities from 100 to 1000 mA·g^{-1}; (**d**) Cycling performance and coulombic efficiency at a current density of 500 mA·g^{-1} for 100 cycles.

To understand the structural evolution in the nanocomposite electrode, the corresponding differential capacity curves for the 1st, 2nd, and 20th charge/discharge cycles are exhibited in Figure 7b. For the Co_3O_4 electrode, the peak at 1.10 V corresponds to its voltage plateau (about 1.10 V) in the first discharge process in Figure 7a. However, this peak position decreases with increasing cycle numbers, indicating that the capacity of the pure Co_3O_4 electrode is unstable. On the other hand, the Co_3O_4/AG nanocomposite shows a good reversibility and cyclability during the process after the first cycle. The differential capacity curve of initial discharge shows three peaks: one profound peak at 0.85 V and two smaller peaks at 1.00 and 1.24 V. The former one is mainly due to the formation of SEI film on the nanocomposite surface and the insertion of lithium-ions into the AG, indicating that the AG in the nanocomposite is beneficial to store lithium-ions. The other two peaks correspond to the reduction reaction of lithium-ions with Co_3O_4, which indicates that the reduction reaction of Co_3O_4 is a multi-step electron capture procedure [54]. Therefore, the reduction reaction can be expressed as the following step [55]:

$$Co_3O_4 + 8Li^+ + 8e^- \rightarrow 3Co + 4Li_2O \tag{1}$$

During the charge process, there are two anodic peaks, corresponding to the two voltage plateaus at 1.30 and 2.10 V in the first charge curve in Figure 7a, which corresponds to the decomposition process of SEI film and the reduction of CoO. During the subsequent discharge processes, the cathodic peaks shift to around 0.87 and 1.4 V and remain unchanged, which suggests that the reversible redox

reaction is gradually built. Additionally, the reversible redox reaction can be expressed as the following steps [56]:

$$CoO + 2Li^+ + 2e^- \leftrightarrow Li_2O + Co, \tag{2}$$

The above results can demonstrate that the electrochemical reaction of the Co_3O_4/AG nanocomposite electrode is irreversible during the first cycle, but a reversible reaction upon the conversion of Co and CoO embedded in the Li_2O matrix is built in the subsequent cycles.

The rate capability of these samples at the current densities of 100 to 1000 $mA \cdot g^{-1}$ is displayed in Figure 7c. Compared to Co_3O_4, the Co_3O_4/AG exhibits a better rate capability, delivering the reversible capacities of 845, 756, 600, and 587 $mAh \cdot g^{-1}$ at current densities of 100, 200, 500, and 1000 $mA \cdot g^{-1}$, respectively. Besides, the performance of this Co_3O_4/AG nanocomposite outperformed that of other Co_3O_4/graphene composites [57,58]. In particular, the reversible capacity returns to 790 $mAh \cdot g^{-1}$ with the decrease of current density to 200 $mA \cdot g^{-1}$, demonstrating the superior recovery ability of the Co_3O_4/AG nanocomposite. Furthermore, the cycling stability of Co_3O_4 and Co_3O_4/AG at a current density of 500 $mA \cdot g^{-1}$ for 100 cycles is shown in Figure 7d. The Co_3O_4/AG exhibits a high initial charge capacity of 570 $mAh \cdot g^{-1}$, which is much higher than that for Co_3O_4 (95 $mAh \cdot g^{-1}$). Meanwhile, the capacity of the nanocomposite is almost constant at 510 $mAh \cdot g^{-1}$ in the subsequent cycles, and the coulombic efficiency is maintained at above 96%; however, the capacity of Co_3O_4 exhibits a constant decrease from the initial capacity of 95 $mAh \cdot g^{-1}$ to 48 $mAh \cdot g^{-1}$ during the 100 cycles. Compared to the capacity of Co_3O_4/carbon aerogel hybrids (478 $mAh \cdot g^{-1}$ at 50 $mA \cdot g^{-1}$), Co_3O_4-NP (400 $mAh \cdot g^{-1}$ at 200 $mA \cdot g^{-1}$), the Co_3O_4/CC@Gr composite (391 $mAh \cdot g^{-1}$ at 100 $mA \cdot g^{-1}$), and block-Co_3O_4/graphene (400 $mAh \cdot g^{-1}$ at 500 $mA \cdot g^{-1}$) [59–62], the cycling performance of the Co_3O_4/AG nanocomposite is comparable and close to the capacity of Co_3O_4 nanowire/graphene (500 $mAh \cdot g^{-1}$ at 1 C) [63] and the Co_3O_4/graphene composite (600 $mAh \cdot g^{-1}$ at 500 $mA \cdot g^{-1}$) [56].

The EIS measurements were applied to obtain insight into the transport kinetics process of the Co_3O_4, AG, and Co_3O_4/AG electrodes. The Nyquist plots of these samples in Figure 8a have a typical semicircle and an inclined line, corresponding to the SEI film, and charge-transfer and lithium-ion diffusion resistance, respectively [64]. As for the AG electrode, it shows the smallest semicircle and the most oblique line compared to Co_3O_4 and Co_3O_4/AG electrodes, indicating that the AG electrode has an excellent electronic conductivity. The size of the semicircle for the Co_3O_4/AG electrode was smaller than that of the Co_3O_4 electrode, which indicates that AG as a substrate can enhance the electronic conductivity of electrode material. In addition, an equivalent electrical circuit was applied to fit the impedance values, and the detailed fitting values are shown in Figure 8b. In brief, the parameters for R_e, R_{sei}, R_{ct}, and W represent the resistance of the electrolyte and electrode, the resistance of the SEI film, the charge transfer resistance, and the Warburg impedance related to lithium ion diffusion, separately [33]. Clearly, the R_e, R_{sei}, and R_{ct} values of the Co_3O_4/AG electrode are smaller than that of Co_3O_4, and it could be found that the R_{total} (116.0 Ω) of the nanocomposite is much lower than that of Co_3O_4 (219.4 Ω), which suggests that the introduction of AG as a substrate could improve the enhanced kinetics of lithium-ions and electronic transport in the nanocomposite electrode. These results could demonstrate that the Co_3O_4/AG nanocomposite as an anode in LIBs possesses high electrical conductivity and excellent reaction kinetics for lithium ions.

The outstanding electrochemical performance of the Co_3O_4/AG nanocomposite could be assigned to two factors: First, the porous nanostructure resulting from AG can shorten the diffusion distance of lithium ions and provide extra active sites to store lithium-ions; meanwhile, a large amount of pores in the AG substrate can relieve the volume change of the Co_3O_4 nanoparticles during the charge/discharge reaction. Second, nitrogen doped in the nanocomposite is conducive to improvement of the electrical conductivity for the nanocomposite. Therefore, the Co_3O_4/AG nanocomposite is a promising anode material in LIB applications.

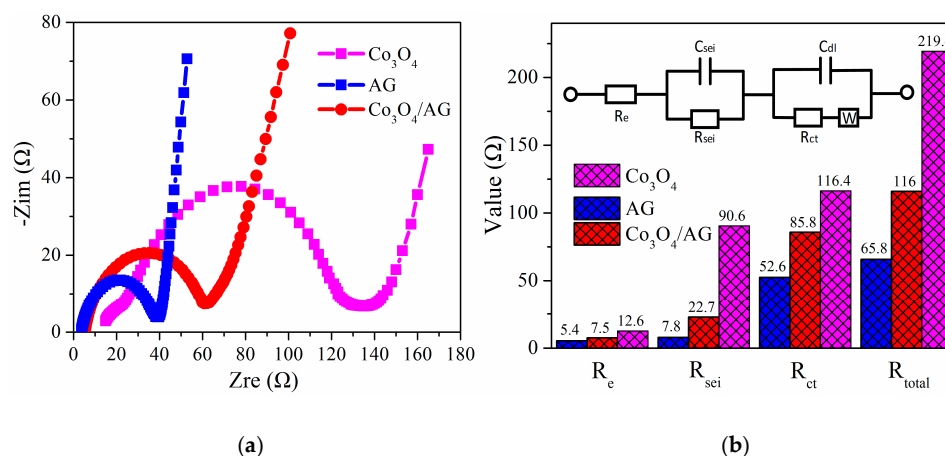**Figure 8.** Electrochemical impedance spectroscopy (EIS) behavior of samples: (**a**) Nyquist plots and (**b**) the values of R_e, R_{sei}, R_{ct}, and R_{total} simulated by the equivalent circuit for Co_3O_4, AG, and the Co_3O_4/AG nanocomposite (inset: the whole equivalent circuit for anode materials).

4. Conclusions

A Co_3O_4/AG nanocomposite was successfully synthesized by the self-assembly of Co_3O_4 nanoparticles in the AG substrate, followed by heat treatment using resource-rich anthracite as the carbonaceous precursor. The Co_3O_4/AG nanocomposite contained uniformly distributed Co_3O_4 nanoparticles with a size smaller than 8 nm on the surface of porous graphene, and had a large specific surface area with well-developed mesopores and a high level of nitrogen doping. This unique Co_3O_4/AG nanocomposite as an anode for LIBs possessed surface-controlled electrode kinetics and a low internal resistance, delivering a better initial reversible capacity of 845 mAh·g^{-1}. Furthermore, a superior cycling stability and rate capability were also achieved. Such an excellent performance results from the unique structure and high conductivity of the nanocomposite. Therefore, the Co_3O_4/AG nanocomposite is a potential anode candidate for large-scale application in LIBs.

Author Contributions: Conceptualization and methodology, H.Z. and B.X.; investigation, H.Z. and B.X.; formal analysis, L.C., G.Y., G.H., and R.Y.; resources, C.Z.; writing—original draft preparation, H.Z. and B.X.; writing—review & editing, Z.C.; project administration and funding acquisition, C.Z. and Y.C.

References

1. Cheng, X.-B.; Zhang, R.; Zhao, C.-Z.; Zhang, Q. Toward safe lithium metal anode in rechargeable batteries: A review. *Chem. Rev.* **2017**, *117*, 10403–10473. [CrossRef] [PubMed]
2. Xu, J.; Wu, J.; Luo, L.; Chen, X.; Qin, H.; Dravid, V.; Mi, S.; Jia, C. Co_3O_4 nanocubes homogeneously assembled on few-layer graphene for high energy density lithium-ion batteries. *J. Power Sources* **2015**, *274*, 816–822. [CrossRef]
3. Blomgren, G.E. The development and future of lithium ion batteries. *J. Electrochem. Soc.* **2017**, *164*, A5019–A5025. [CrossRef]
4. Yang, Y.; Huang, J.; Zeng, J.; Xiong, J.; Zhao, J. Direct Electrophoretic Deposition of Binder-Free Co_3O_4/Graphene Sandwich-Like Hybrid Electrode as Remarkable Lithium Ion Battery Anode. *ACS Appl. Mater. Interfaces* **2017**, *9*, 32801–32811. [CrossRef] [PubMed]

5.　Zhou, L.; Zhang, K.; Hu, Z.; Tao, Z.; Mai, L.; Kang, Y.M.; Chou, S.L.; Chen, J. Recent Developments on and Prospects for Electrode Materials with Hierarchical Structures for Lithium-Ion Batteries. *Adv. Energy Mater.* **2018**, *8*, 1701415. [CrossRef]

6.　Zubi, G.; Dufo-López, R.; Carvalho, M.; Pasaoglu, G. The lithium-ion battery: State of the art and future perspectives. *Renew. Sustain. Energy Rev.* **2018**, *89*, 292–308. [CrossRef]

7.　Gu, L.; Xie, W.; Bai, S.; Liu, B.; Xue, S.; Li, Q.; He, D. Facile fabrication of binder-free NiO electrodes with high rate capacity for lithium-ion batteries. *Appl. Surf. Sci.* **2016**, *368*, 298–302. [CrossRef]

8.　Sun, M.; Sun, M.; Yang, H.; Song, W.; Nie, Y.; Sun, S. Porous Fe_2O_3 nanotubes as advanced anode for high performance lithium ion batteries. *Ceram. Int.* **2017**, *43*, 363–367. [CrossRef]

9.　Jiang, Y.; Yue, J.L.; Guo, Q.; Xia, Q.; Zhou, C.; Feng, T.; Xu, J.; Xia, H. Highly Porous Mn_3O_4 Micro/Nanocuboids with In Situ Coated Carbon as Advanced Anode Material for Lithium-Ion Batteries. *Small* **2018**, *14*, 1704296. [CrossRef]

10.　Hu, Y.; Yan, C.; Chen, D.; Lv, C.; Jiao, Y.; Chen, G. One-dimensional Co_3O_4 nanonet with enhanced rate performance for lithium ion batteries: Carbonyl-β-cyclodextrin inducing and kinetic analysis. *Chem. Eng. J.* **2017**, *321*, 31–39. [CrossRef]

11.　Zhao, Y.; Li, X.; Yan, B.; Xiong, D.; Li, D.; Lawes, S.; Sun, X. Recent Developments and Understanding of Novel Mixed Transition-Metal Oxides as Anodes in Lithium Ion Batteries. *Adv. Energy Mater.* **2016**, *6*, 1502175. [CrossRef]

12.　Zheng, M.; Tang, H.; Li, L.; Hu, Q.; Zhang, L.; Xue, H.; Pang, H. Hierarchically Nanostructured Transition Metal Oxides for Lithium-Ion Batteries. *Adv. Sci.* **2018**, *5*, 1700592. [CrossRef] [PubMed]

13.　Sharma, J.K.; Srivastava, P.; Singh, G.; Akhtar, M.S.; Ameen, S. Green synthesis of Co_3O_4 nanoparticles and their applications in thermal decomposition of ammonium perchlorate and dye-sensitized solar cells. *Mater. Sci. Eng. B* **2015**, *193*, 181–188. [CrossRef]

14.　Rai, A.K.; Gim, J.; Anh, L.T.; Kim, J. Partially reduced Co_3O_4/graphene nanocomposite as an anode material for secondary lithium ion battery. *Electrochim. Acta* **2013**, *100*, 63–71. [CrossRef]

15.　Hu, R.; Zhang, H.; Bu, Y.; Zhang, H.; Zhao, B.; Yang, C. Porous Co_3O_4 nanofibers surface-modified by reduced graphene oxide as a durable, high-rate anode for lithium ion battery. *Electrochim. Acta* **2017**, *228*, 241–250. [CrossRef]

16.　Wu, H.B.; Chen, J.S.; Hng, H.H.; Lou, X.W.D. Nanostructured metal oxide-based materials as advanced anodes for lithium-ion batteries. *Nanoscale* **2012**, *4*, 2526–2542. [CrossRef] [PubMed]

17.　Poizot, P.; Laruelle, S.; Grugeon, S.; Dupont, L.; Tarascon, J.M. Nano-sized transition-metal oxides as negative-electrode materials for lithium-ion batteries. *Nature* **2000**, *407*, 496–499. [CrossRef]

18.　Park, J.S.; Shin, D.O.; Lee, C.S.; Lee, Y.-G.; Kim, J.Y.; Kim, K.M.; Shin, K. Mesoporous perforated Co_3O_4 nanoparticles with a thin carbon layer for high performance Li-ion battery anodes. *Electrochim. Acta* **2018**, *264*, 376–385. [CrossRef]

19.　Li, J.; Li, Z.; Ning, F.; Zhou, L.; Zhang, R.; Shao, M.; Wei, M. Ultrathin Mesoporous Co_3O_4 Nanosheet Arrays for High-Performance Lithium-Ion Batteries. *ACS Omega* **2018**, *3*, 1675–1683. [CrossRef]

20.　Chen, Y.; Wang, Y.; Yang, H.; Gan, H.; Cai, X.; Guo, X.; Xu, B.; Lü, M.; Yuan, A. Facile synthesis of porous hollow Co_3O_4 microfibers derived-from metal-organic frameworks as an advanced anode for lithium ion batteries. *Ceram. Int.* **2017**, *43*, 9945–9950. [CrossRef]

21.　Meng, Y.; Wang, G.; Xiao, M.; Duan, C.; Wang, C.; Zhu, F.; Zhang, Y. Ionic liquid-derived Co_3O_4/carbon nano-onions composite and its enhanced performance as anode for lithium-ion batteries. *J. Mater. Sci.* **2017**, *52*, 13192–13202. [CrossRef]

22.　Gu, D.; Li, W.; Wang, F.; Bongard, H.; Spliethoff, B.; Schmidt, W.; Weidenthaler, C.; Xia, Y.; Zhao, D.; Schuth, F. Controllable Synthesis of Mesoporous Peapod-like Co_3O_4@Carbon Nanotube Arrays for High-Performance Lithium-Ion Batteries. *Angew. Chem. Int. Ed.* **2015**, *54*, 7060–7064. [CrossRef] [PubMed]

23.　Wang, L.; Zheng, Y.; Wang, X.; Chen, S.; Xu, F.; Zuo, L.; Wu, J.; Sun, L.; Li, Z.; Hou, H.; et al. Nitrogen-Doped Porous Carbon/Co_3O_4 Nanocomposites as Anode Materials for Lithium-Ion Batteries. *ACS Appl. Mater. Interfaces* **2014**, *6*, 7117–7125. [CrossRef] [PubMed]

24. Vaqueiro-Contreras, M.; Bartlam, C.; Bonilla, R.; Markevich, V.; Halsall, M.; Vijayaraghavan, A.; Peaker, A. Graphene oxide films for field effect surface passivation of silicon for solar cells. *Sol. Energy Mater. Sol. Cells* **2018**, *187*, 189–193. [CrossRef]

25. Ma, C.; Zhao, Y.; Li, Y. A facile solution-free etching preparation of porous graphene nanosheets with high performances for lithium storage. *Chem. Eng. J.* **2017**, *320*, 283–289. [CrossRef]

26. Sun, H.; Liu, Y.; Yu, Y.; Ahmad, M.; Nan, D.; Zhu, J. Mesoporous Co_3O_4 nanosheets-3D graphene networks hybrid materials for high-performance lithium ion batteries. *Electrochim. Acta* **2014**, *118*, 1–9. [CrossRef]

27. Zhou, Q.; Zhao, Z.; Zhang, Y.; Meng, B.; Zhou, A.; Qiu, J. Graphene Sheets from Graphitized Anthracite Coal: Preparation, Decoration, and Application. *Energy Fuels* **2012**, *26*, 5186–5192. [CrossRef]

28. He, X.; Li, X.; Ma, H.; Han, J.; Zhang, H.; Yu, C.; Xiao, N.; Qiu, J. ZnO template strategy for the synthesis of 3D interconnected graphene nanocapsules from coal tar pitch as supercapacitor electrode materials. *J. Power Sources* **2017**, *340*, 183–191. [CrossRef]

29. Gao, F.; Qu, J.; Zhao, Z.; Zhou, Q.; Li, B.; Qiu, J. A green strategy for the synthesis of graphene supported Mn_3O_4 nanocomposites from graphitized coal and their supercapacitor application. *Carbon* **2014**, *80*, 640–650. [CrossRef]

30. Xing, B.; Zeng, H.; Huang, G.; Zhang, C.; Yuan, R.; Cao, Y.; Chen, Z.; Yu, J. Porous graphene prepared from anthracite as high performance anode materials for lithium-ion battery applications. *J. Alloys Compd.* **2018**, *779*, 202–211. [CrossRef]

31. Rivas Murias, B.; Salgueiriño, V. Thermodynamic $CoO-Co_3O_4$ crossover using Raman spectroscopy in magnetic octahedron-shaped nanocrystals. *J. Raman Spectrosc.* **2017**, *48*, 837–841. [CrossRef]

32. Deng, X.; Li, J.; Zhu, S.; He, F.; He, C.; Liu, E.; Shi, C.; Li, Q.; Zhao, N. Metal-organic frameworks-derived honeycomb-like Co_3O_4/three-dimensional graphene networks/Ni foam hybrid as a binder-free electrode for supercapacitors. *J. Alloys Compd.* **2017**, *693*, 16–24. [CrossRef]

33. Zhang, Y.; Li, Y.; Chen, J.; Zhao, P.; Li, D.; Mu, J.; Zhang, L. CoO/Co_3O_4/graphene nanocomposites as anode materials for lithium-ion batteries. *J. Alloys Compd.* **2017**, *699*, 672–678. [CrossRef]

34. Zhang, P.; Han, X.; Hu, H.; Gui, J.; Li, M.; Qiu, J. In-situ growth of highly uniform and single crystalline Co_3O_4 nanocubes on graphene for efficient oxygen evolution. *Catal. Commun.* **2017**, *88*, 81–84. [CrossRef]

35. Guo, S.; Feng, Y.; Ding, W.; Li, X.; Yang, L.; Yao, J. Design of porous Co_3O_4 nanosheets via one-step synthesis as high-performance anode materials for lithium-ion batteries. *J. Solid State Electrochem.* **2018**, *23*, 1–7. [CrossRef]

36. Li, L.; Zhou, G.; Shan, X.-Y.; Pei, S.; Li, F.; Cheng, H.-M. Co_3O_4 mesoporous nanostructures@ graphene membrane as an integrated anode for long-life lithium-ion batteries. *J. Power Sources* **2014**, *255*, 52–58. [CrossRef]

37. Su, Q.; Yuan, W.; Yao, L.; Wu, Y.; Zhang, J.; Du, G. Microwave-assisted synthesis of Co_3O_4–graphene sheet-on-sheet nanocomposites and electrochemical performances for lithium ion batteries. *Mater. Res. Bull.* **2015**, *72*, 43–49. [CrossRef]

38. Wang, Y.; Ma, R.; Liu, L.; Xu, Z.; Li, F. A Facile One-Pot Method for Co_3O_4/Graphene Composite as Efficient Electrode Materials for Supercapacitors. *Nano* **2017**, *12*, 1750102. [CrossRef]

39. Liao, Y.; Huang, Y.; Shu, D.; Zhong, Y.; Hao, J.; He, C.; Zhong, J.; Song, X. Three-dimensional nitrogen-doped graphene hydrogels prepared via hydrothermal synthesis as high-performance supercapacitor materials. *Electrochim. Acta* **2016**, *194*, 136–142. [CrossRef]

40. Wang, H.; Zhang, C.; Liu, Z.; Wang, L.; Han, P.; Xu, H.; Zhang, K.; Dong, S.; Yao, J.; Cui, G. Nitrogen-doped graphene nanosheets with excellent lithium storage properties. *J. Mater. Chem.* **2011**, *21*, 5430. [CrossRef]

41. Ma, G.; Huang, K.; Zhuang, Q.; Ju, Z. Superior cycle stability of nitrogen-doped graphene nanosheets for Na-ion batteries. *Mater. Lett.* **2016**, *174*, 221–225. [CrossRef]

42. Jin, Y.; Wang, L.; Shang, Y.; Gao, J.; Li, J.; He, X. Facile synthesis of monodisperse Co_3O_4 mesoporous microdisks as an anode material for lithium ion batteries. *Electrochim. Acta* **2015**, *151*, 109–117. [CrossRef]

43. Leng, M.; Huang, X.; Xiao, W.; Ding, J.; Liu, B.; Du, Y.; Xue, J. Enhanced oxygen evolution reaction by Co-O-C bonds in rationally designed Co_3O_4/graphene nanocomposites. *Nano Energy* **2017**, *33*, 445–452. [CrossRef]

44. Luo, L.; Wu, J.; Xu, J.; Dravid, V.P. Atomic Resolution Study of Reversible Conversion Reaction in Metal Oxide Electrodes for Lithium-Ion Battery. *ACS Nano* **2014**, *8*, 11560–11566. [CrossRef] [PubMed]

45. Su, Q.; Zhang, J.; Wu, Y.; Du, G. Revealing the electrochemical conversion mechanism of porous Co₃O₄ nanoplates in lithium ion battery by in situ transmission electron microscopy. *Nano Energy* **2014**, *9*, 264–272. [CrossRef]

46. Yu, M.; Sun, Y.; Du, H.; Wang, C.; Li, W.; Dong, R.; Sun, H.; Geng, B. Hollow porous carbon spheres doped with a low content of Co₃O₄ as anode materials for high performance lithium-ion batteries. *Electrochim. Acta* **2019**, *317*, 562–569. [CrossRef]

47. Li, H.-H.; Zhou, L.; Zhang, L.-L.; Fan, C.-Y.; Fan, H.-H.; Wu, X.-L.; Sun, H.-Z.; Zhang, J.-P. Co₃O₄ Nanospheres Embedded in a Nitrogen-Doped Carbon Framework: An Electrode with Fast Surface-Controlled Redox Kinetics for Lithium Storage. *ACS Energy Lett.* **2016**, *2*, 52–59. [CrossRef]

48. Yuan, T.; Jiang, Y.; Sun, W.; Xiang, B.; Li, Y.; Yan, M.; Xu, B.; Dou, S. Ever-Increasing Pseudocapacitance in RGO-MnO-RGO Sandwich Nanostructures for Ultrahigh-Rate Lithium Storage. *Adv. Funct. Mater.* **2016**, *26*, 2198–2206. [CrossRef]

49. Chen, M.; Xia, X.; Yin, J.; Chen, Q. Construction of Co₃O₄ nanotubes as high-performance anode material for lithium ion batteries. *Electrochim. Acta* **2015**, *160*, 15–21. [CrossRef]

50. Sun, F.; Huang, K.; Qi, X.; Gao, T.; Liu, Y.; Zou, X.; Zhong, J. Enhanced 3D hierarchical double porous Co₃O₄/graphene architecture for superior rechargeable lithium ion battery. *Ceram. Int.* **2014**, *40*, 2523–2528. [CrossRef]

51. Wang, D.; Yu, Y.; He, H.; Wang, J.; Zhou, W.; Abruna, H.D. Template-free synthesis of hollow-structured Co₃O₄ nanoparticles as high-performance anodes for lithium-ion batteries. *ACS Nano* **2015**, *9*, 1775–1781. [CrossRef] [PubMed]

52. Yao, Y.; Zhu, Y.; Zhao, S.; Shen, J.; Yang, X.; Li, C. Halide Ion Intercalated Electrodeposition Synthesis of Co₃O₄ Nanosheets with Tunable Pores on Graphene Foams as Free-Standing and Flexible Li-Ion Battery Anodes. *ACS Appl. Energy Mater.* **2018**, *1*, 1239–1251. [CrossRef]

53. Long, H.; Zhang, M.; Wang, Q.; Xing, L.; Wang, S.; Xue, X. Plasma-treated Co₃O₄/graphene nanocomposite as high performance anode of lithium-ion battery. *J. Alloy. Compd.* **2017**, *701*, 200–207. [CrossRef]

54. Hu, C.; Guo, J.; Wen, J.; Peng, Y. Preparation and Electrochemical Performance of Nano-Co₃O₄ Anode Materials from Spent Li-Ion Batteries for Lithium-Ion Batteries. *J. Mater. Sci. Technol.* **2013**, *29*, 215–220. [CrossRef]

55. Yang, Q.; Wu, J.; Huang, K.; Lei, M.; Wang, W.; Tang, S.; Lu, P.; Lu, Y.; Liu, J. Layer-by-layer self-assembly of graphene-like Co₃O₄ nanosheet/graphene hybrids: Towards high-performance anode materials for lithium-ion batteries. *J. Alloy. Compd.* **2016**, *667*, 29–35. [CrossRef]

56. Chi, X.; Chang, L.; Xie, D.; Zhang, J.; Du, G. Hydrothermal preparation of Co₃O₄/graphene composite as anode material for lithium-ion batteries. *Mater. Lett.* **2013**, *106*, 178–181. [CrossRef]

57. Wu, Z.-S.; Ren, W.; Wen, L.; Gao, L.; Zhao, J.; Chen, Z.; Zhou, G.; Li, F.; Cheng, H.-M. Graphene Anchored with Co₃O₄ Nanoparticles as Anode of Lithium Ion Batteries with Enhanced Reversible Capacity and Cyclic Performance. *ACS Nano* **2010**, *4*, 3187–3194. [CrossRef]

58. Yang, X.; Fan, K.; Zhu, Y.; Shen, J.; Jiang, X.; Zhao, P.; Luan, S.; Li, C. Electric Papers of Graphene-Coated Co₃O₄ Fibers for High-Performance Lithium-Ion Batteries. *ACS Appl. Mater. Interfaces* **2013**, *5*, 997–1002. [CrossRef]

59. Hao, F.; Zhang, Z.; Yin, L. Co₃O₄/Carbon Aerogel Hybrids as Anode Materials for Lithium-Ion Batteries with Enhanced Electrochemical Properties. *ACS Appl. Mater. Interfaces* **2013**, *5*, 8337–8344. [CrossRef]

60. Zhao, Y.; Li, Y.; Ma, C.; Shao, Z. Micro-/nano-structured hybrid of exfoliated graphite and Co₃O₄ nanoparticles as high-performance anode material for Li-ion batteries. *Electrochim. Acta* **2016**, *213*, 98–106. [CrossRef]

61. Xie, Q.; Zhang, Y.; Zhu, Y.; Fu, W.; Zhang, X.; Zhao, P.; Wu, S. Graphene enhanced anchoring of nanosized Co₃O₄ particles on carbon fiber cloth as free-standing anode for lithium-ion batteries with superior cycling stability. *Electrochim. Acta* **2017**, *247*, 125–131. [CrossRef]

62. Shao, J.; Zhou, H.; Zhu, M.; Feng, J.; Yuan, A. Facile synthesis of metal-organic framework-derived Co₃O₄ with different morphologies coated graphene foam as integrated anodes for lithium-ion batteries. *J. Alloys Compd.* **2018**, *768*, 1049–1057. [CrossRef]

63. Kim, Y.; Noh, Y.; Han, H.; Bae, J.; Park, S.; Lee, S.; Yoon, W.; Kim, Y.K.; Ahn, H.; Ham, M.-H.; et al. Effect of N-doped carbon layer on Co_3O_4 nanowire-graphene composites as anode materials for lithium ion batteries. *J. Phys. Chem. Solids* **2019**, *124*, 266–273. [CrossRef]

64. Zhai, X.; Xu, X.; Zhu, X.; Zhao, Y.; Li, J.; Jin, H. Porous layer assembled hierarchical Co_3O_4 as anode materials for lithium-ion batteries. *J. Mater. Sci.* **2018**, *53*, 1356–1364. [CrossRef]